Load assessment of a wind farm considering negative and positive yaw misalignment for wake steering

Regis Thedin[1], Garrett Barter[1], Jason Jonkman[1], Rafael Mudafort[1], Chris Bay[1], Kelsey Shaler[2], and Jasper Kreeft[3]

[1]National Renewable Energy Laboratory, Golden, CO, USA
[2]Shell International Exploration and Production, Houston, TX, USA
[3]Shell Global Solutions International B.V., The Hague, Netherlands

Correspondence: Regis Thedin (regis.thedin@nrel.gov)

Abstract. Wake steering strategies are employed to increase the overall power production of wind farms by deflecting wakes of upstream turbines away from downstream ones. The gain in net power comes at the expense of increased fatigue loads experienced by downstream turbines. In this work we investigate performance and fatigue loading characteristics of a small farm consisting of five aligned IEA Wind 15-MW wind turbines. A parametric study is performed where, for every wind direction from −20 to 20 degrees, the yaw misalignment angle varies from −25 to 25 degrees. This setup allowed us to investigate asymmetries and identify optimal conditions for a given wind direction. In general, we found that positive yaw configurations are preferred and that yaw configurations that result in attractive power gains (25% or more when compared to a baseline no-yaw scenario) come with significant increase in fatigue loading (we used standard deviation and damage-equivalent load (DEL) of the blade-root, low-speed shaft, and tower-base moments as proxies for fatigue load). We found that for any given positive wind inflow angle, yaw angles between −2.5 and 15 degrees yield power gains of 10–20% over a no-yaw baseline, and positive yaw is preferred because of lower fatigue loadings. For any given negative wind inflow angles, positive yaw also results in lower magnitudes of standard deviation and DEL for the channels investigated. A small power loss of up to 2% is observed for some positive yaw angles under negative wind directions (as compared symmetric negative yaw and positive wind cases), but gains in terms of loads exceed 25% and may be enough to justify a positive yaw configuration under negative winds as well. We show that such behavior can be explained by partial waking and the direction of rotation of the rotor.

1 Introduction

Deflecting or dissipating wind turbine wakes within a larger array is a recognized strategy to increase wind farm energy yields. In the case of wake steering, upstream turbines are yaw misaligned with the incoming flow such that their wakes are deflected away from downstream turbines. While the upstream turbine produces slightly less power than it would otherwise, the downstream turbines see higher inflow velocity and the net power production of the array increases. Exploring the benefits and operational dynamics of wake steering has been an active field of research over the past 10–15 years via simulation (Medici and Dahlberg, 2003a; Jiménez et al., 2010; Fleming et al., 2014; Gebraad et al., 2016), wind tunnel experiments (Bastankhah

and Porté-Agel, 2019; Adaramola and Krogstad, 2011; Medici and Dahlberg, 2003b; Medici and Alfredsson, 2006; Wagenaar
25   et al., 2012), and field test trials (Fleming et al., 2017, 2019, 2020; Doekemeijer et al., 2020; Simley et al., 2021). Houck (2021)
offers a nice review of the literature.

In their simplest form, wind farm controllers might dial-in optimal yaw settings to every turbine in the array based on a
precomputed library of inflow conditions. With more sophistication, farm controllers might make collective adjustments based
on real-time observations and turbine condition monitoring. Regardless of its level of sophistication, the farm controller will
30   have to account for a fundamental asymmetry in wake deflection physics. The asymmetries are primarily due to the clockwise
rotation standard of the rotor (when viewed "head-on"), but also likely a result of the atmospheric conditions (e.g. veer due
to Coriolis forces). This makes positive angle yaw deflections (counter-clockwise when viewed from above) more effective
than negative angle displacements (clockwise from above). The physical mechanisms of this asymmetry are well explained by
Bastankhah and Porté-Agel (2016) and Hulsman et al. (2022). A diagram of the conventions used is shown in Fig. 1.
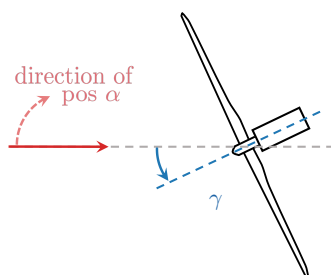
Figure 1. Wind turbine viewed from above, showing the conventions used. Shown is a positively yawed turbine under aligned (zero degrees)
wind.

35   That being said, the negative angle yaw settings could still be used for inflow scenarios where the wind direction alignment
relative to the turbine array creates partial wakes in the direction of negative yaw misalignment, so additional negative yaw
deflection is the optimal approach.

As wake steering reaches commercial maturity, it is critical that its impact on operational loading is well understood so that
farm control algorithms can be devised that maximize energy production while limiting turbine structural loads. The impact of
40   wake steering on turbine loading has been, and continues to be, an important focus because intentional yaw misalignments and
partial waking are not part of the turbine design standards. Furthermore, turbine manufacturers, project developers, and wind
farm owner-operators will be wary of adopting wake steering strategies if they lead to increased maintenance costs or shorter
turbine lifetimes.

The consensus in the literature is that for most load quantities of interest, the loads on the front row turbines decrease with
45   wake steering while the loads on the downstream turbines increase. This is due to the decrease in power production and rotor
thrust in the front row turbines, with a corresponding increase in the downstream turbines, relative to the no-wake steering
scenario (Kanev et al., 2020; Shaler et al., 2022). This brings loading values into a more consistent level across the array, which
could have maintenance planning and cost advantages. While this might be a general trend, there are exceptions, such as tower

or monopile yaw moments, which increase with any yaw misalignment. Because wake steering is generally applied below rated wind speeds, any increase in loading is unlikely to approach the ultimate load operational envelope of the turbine, but fatigue loading and turbine lifetime is of concern. The impact on fatigue and turbine lifetime will be dependent on the frequency of wake steering (Shaler et al., 2022). There is also consensus that imperfect wake steering that exacerbates the presence of partial waking could be even more harmful than not employing wake steering at all (Ciri et al., 2018; Stanley et al., 2020).

In terms of positive vs negative yaw angles, one might think that turbine load behavior would mimic that of power production. Meaning, that turbine loads (whether measured by mean loading, fatigue loading, or ultimate loading) would show similar trends regardless of the direction of yaw, with some allowance for slight asymmetry due to the clockwise rotation of the rotor. However, prior work suggests that this might not always be the case. Damiani et al. (2018) compared elastic simulations with in-situ instrumentation of a General Electric (GE) 1.5sle 1.5-megawatt (MW) wind turbine and noted asymmetries related to positive and negative yaw directions. Ennis et al. (2018) similarly used field tests of a three-turbine array to demonstrate preferential direction for yaw misalignments for blade flap and edge loading. Zalkind and Pao (2016) also reported asymmetric trends in simulation-based study of the NREL 5-MW reference wind turbine. In these papers, some load statistics showed monotonically increasing or decreasing behavior when sweeping from negative to positive yaw offset angles.

This work intends to understand the load asymmetries across positive vs negative yaw angles to arrive at operational recommendations for wind farm owners. We learn from the range of conditions examined by Shaler et al. (2022) to focus our computational simulations on a five-turbine array with a systematic exploration of incoming wind direction and yaw angle at set values for freestream velocity, shear profile, and turbulence intensity. We ensure that the modeling fidelity and verification are sufficient to capture the curled ("kidney bean shaped") wake physics that are important to the asymmetries. We indeed observe asymmetric loading and arrive at recommendations based on the "quadrants" of positive and negative incoming wind direction angles (relative to the array alignment) compared to positive and negative yaw misalignments for wake steering.

2 Methodology

In this work, we investigate power performance and load response of a small wind farm when subject to positive and negative yaw misalignments. A parametric study of different yaw angles under different wind directions is performed using the mid-fidelity wind plant performance tool, FAST.Farm. A pre-processing calibration step is taken to ensure the FAST.Farm wake characteristics, including its curled shape, match those obtained using high-fidelity large-eddy simulation (LES) results.

2.1 Computational Models

The high-fidelity LES simulations are executed using ExaWind's AMR-Wind code (Sprague et al., 2020). AMR-Wind is a massively parallel, incompressible flow solver tailored for wind energy applications. The primary application of AMR-Wind in this work is to perform LES of an atmospheric boundary layer, and simulate turbine wakes using an actuator line model for the turbine representation. AMR-Wind is only used for the calibration step, which will be described in Section 3.

80   After calibration, the majority of results in this work are obtained using FAST.Farm. FAST.Farm is a multiphysics engineering tool for predicting the power performance and structural load response of wind turbines within a wind farm. For each turbine, FAST.Farm uses individual OpenFAST instances to solve for the aero-hydro-servo-elastic dynamics. Information about the ambient wind are given as inputs to FAST.Farm–that is, it does not fully resolve all fluid flow equations. Wake deficits, advection, deflection, meandering, and merging are all handled by dynamic wake meandering models within FAST.Farm. The

85   inflow conditions are given in terms of small, high-resolution boxes around each turbine, and one large, lower-resolution box around the entire farm. The high-resolution boxes are responsible for providing inflow conditions to OpenFAST for aero-elastic analysis, while the low-resolution box meanders the wake. Due to its computational cost and level of accuracy, FAST.Farm is considered an engineering-fidelity tool to support detailed design and loads analysis of wind turbines in a farm context. More details of FAST.Farm can be found in Jonkman et al. (2017).

90   The approach of using an engineering-fidelity tool (after a proper calibration against high-fidelity LES) is due to computational cost and speed. A single LES case executed using AMR-Wind and used for calibration take up to about 2.5 days on a high-performance computing environment, using around 2,800 cores. That is not including a precursor simulation, which will take an additional 1 to 1.5 days on around 750 cores. Similarly, each FAST.Farm case executed in this work takes about 3 to 4 hours on 5 cores only. The calibration step is important in ensuring the wake characteristics matches those of the LES for

95   the same condition; they were, however, the most computationally expensive step of this work. The calibration performed here allows us to re-utilize, in future studies, the values obtained.

2.2 Case Study Setup

For this study we devise a small wind farm consisting of 5 aligned IEA Wind 15-MW reference wind turbines (Gaertner et al., 2020). All OpenFAST instances of turbines within FAST.Farm in this work use the same controller, based on the reference

100   open-source controller ROSCO (Abbas et al., 2022). The turbines are spaced by 1 nautical mile, or approximately 7.7 diameters, inspired by the projects in active development in Massachusetts waters. The goal is to perform a parametric study varying the wind direction and the yaw angle of the 5 turbines in the following fashion:

   – Vary wind direction, α, from -10 to 10 degrees, in increments of 2 degrees.

   – For each wind direction α, vary the reference yaw misalignment angle, γ, from -25 to 25 degrees in increments of 2.5

105   degrees. For each value of the reference γ, the yaw misalignment for the 5 turbines are such that $\gamma_{T1} = \gamma_{T2} = \gamma_{T3} = \gamma$, $\gamma_{T4} = \gamma/2$ and $\gamma_{T5} = 0$.

We limit the yaw misalignment to a magnitude of 25 degrees due to the higher structural loads that such conditions impose (Damiani et al., 2018; Shaler et al., 2022). The yaw angles for each of the five turbines are considered to be realistic, such as zero yaw angle for the last turbine in the row, based on prior literature where yaw angles of a row of 5 turbines have been

110   investigated Bastankhah and Porté-Agel (2019). We keep the same magnitudes for positive and negative yaw to allow direct comparison, rather than using optimized angles for each scenario. In the figures presented in this work, we will refer to the different yaw cases simply by the reference yaw γ. Given the farm layout, instead of generating new wind fields for each wind

direction, we opt to rotate the farm. This way we ensure that the wind fields for the leading turbine are the same used in all cases, and more consistent turbine response across the different cases (some quantities are normalized by the leading turbine).

115 An illustration of the complete setup, including the farm layout for each different wind direction is given in Figure 2.
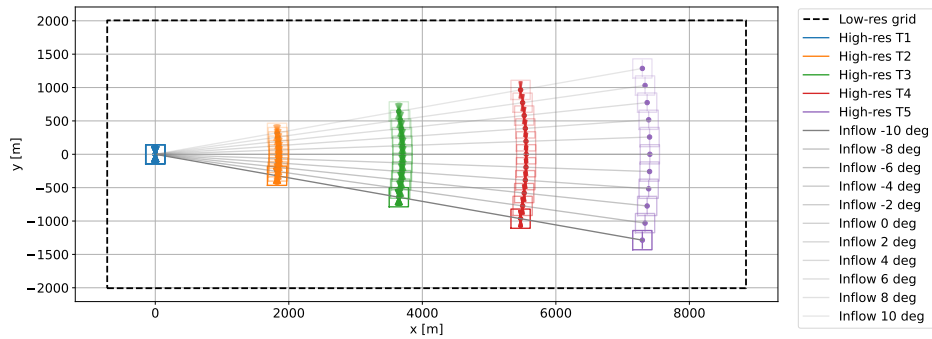
Figure 2. Illustration of the farm layout setup for FAST.Farm. The low-resolution and all the high-resolution domains are shown. Each gray line represents one inflow direction. All the yaw positions considered for each turbine are shown; note how last turbine is always at zero yaw.

The layout shown in Figure 2 includes all the cases at once. Each individual case, consisting of a certain wind direction α and yaw γ can be obtained through a trivial change in reference frames. Figure 3 demonstrates the change in reference frame. The flowfield figures presented in this paper will be shown in the style of Figure 3(b).
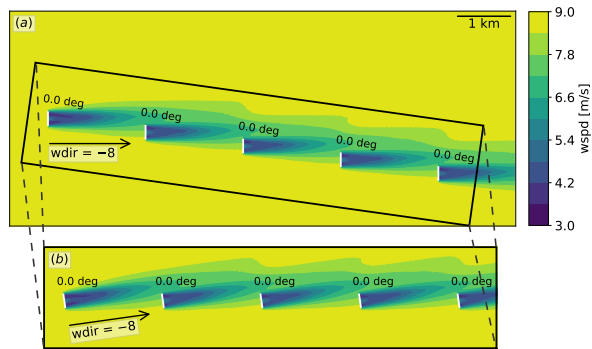
Figure 3. Change in reference frame to use the same wind fields for different wind directions. (a) Following reference of Figure 2, a solution at wind direction $\alpha = -8$ and yaw angles $\gamma = 0$; (b) Rotated reference to a more intuitive layout given wind direction and yaw angles. All the flowfield pictures presented here will be shown using the rotated frame of reference shown in (b).

2.3 Inflow Generation

120 The focus of this study is on a single wind condition. Our interests lie in the differences observed in terms of power and loads for different wind directions and different yaw misalignment. We have selected a wind speed of 8.6 m/s, representing a below-rated, "Region II" operation of the IEA Wind 15-MW reference wind turbine.

Turbulent wind fields are complex and difficult to model accurately. Large-eddy simulation tools are able to resolve the larger eddies up to the grid resolution, while the smaller, sub-grid, eddies are modeled. Such simulations require intensive computa-
125 tional resources, and are considered the high-fidelity "truth" in this work. Engineering-fidelity models of the wind inflow are available where the wind fields have the appropriate second-order statistics, but are not able to recreate true turbulence eddies and their coherent structure. One of the main underlying assumptions of these models is that most do not consider buoyancy, leading to significant inaccuracies when used for non-neutral scenarios.

For the calibration of FAST.Farm, we generated an inflow velocity field using the AMR-Wind LES model. This allowed
130 for direct comparison between the two codes and ensured that the parameters for the dynamic wake meandering model within FAST.Farm are as accurate as possible for the conditions under investigation. After the calibration step, for the parametric study of turbine loads based on inflow wind direction and yaw angles, we model the flowfields using TurbSim (Kelley and Jonkman, 2005), a synthetic turbulence generator based on the Kaimal spectrum model with Davenport's exponential coherence model, which assumes neutral atmospheric stability. We tuned the TurbSim inputs to mimic the LES turbulence statistics.

135 In generating the LES inflow, we specify our desired wind speed (8.6 m/s) at the desired height (150 m), as well as parameters such as ground heat flux (0 K-m/s for neutral stability), surface roughness (0.75 m), capping inversion height (750 m) and strength (10 K across 100 m). Our domain is large to avoid deep array effects once we add the turbines, coming to a $10 \times 7.5 \times 1$ km extent. The turbulence intensity and shear exponents are not inputs, but rather a result of the combination of physical drivers and require an iterative process (varying the aforementioned parameters), to achieve target statistics. The values listed above
140 were the final ones used such that we obtained our target quantities. The simulation is executed for 1800 s after it reaches a quasi-stationary state. The resulting atmospheric boundary layer for the period of interest has a mean shear exponent of 0.196, a mean TI of 10%, and a friction velocity of 0.54 m/s. A low veer, typical of neutral conditions, is obtained, at 0.011 degrees/m. The final vertical profiles of the boundary layer are shown in Figure 4.

The canonical condition obtained through LES (10% turbulence intensity and 0.2 shear exponent) is also specified within
145 TurbSim after the calibration step for the batch runs. We acknowledge that while using TurbSim is appropriate for the conditions of interest of this work, it would incur larger model errors if the condition of interest included non-neutral atmospheric stratification.

2.4 Quantities of interest

Wind farm performance and loads are the main interest in this work. With the power gains due to wake steering, the turbine
150 components are typically subject to increased fatigue loads. The selected load channels that will be investigated are outlined in Table 1 and processed in terms of quantities used as a proxy for fatigue loads.

Fatigue is the damage that accumulates in structural components over time due to cyclic loadings. Such damaging effect can be modeled using the S-N curve, which indicates the amount of cycles a structure can endure until it fails for a given cyclic stress. The slope of this curve is the Wöhler exponent. We can frame the concept of damage related to fatigue loads in terms
155 of an equivalent fatigue load. A load of equivalent fatigue damage, commonly referred to as damage equivalent load (DEL)
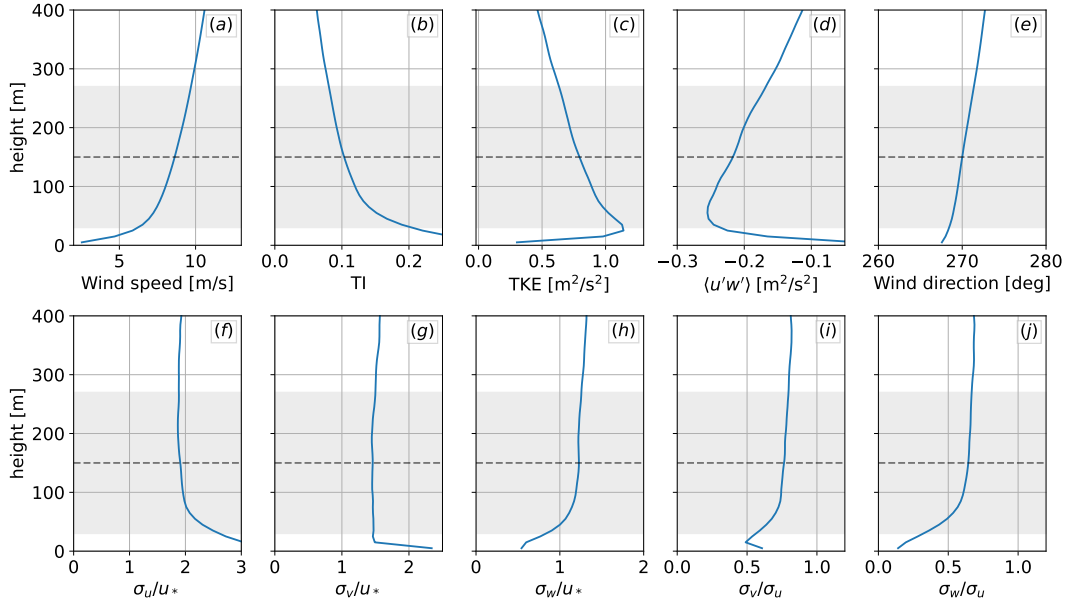
Figure 4. Planar- and time-average vertical profiles of several quantities of a neutral atmosphere simulated using LES. Rotor swept zone shown for reference with gray shading. (a) Wind speed; (b) turbulence intensity; (c) turbulent kinetic energy; (d) vertical flux of the streamwise component of the wind; (e) wind direction; (f,g,h) variance of the streamwise, lateral, and vertical component of the wind normalized by the friction velocity, respectively; (i,j) ratio of the variance of the lateral and vertical component of the wind to the streamwise component, respectively.

Table 1. Description of the load channels of interest.

Channel	Description
Blade root bending moment	Magnitude of the combined blade root out-of-plane bending moment (flapwise) and in-plane bending moment (edgewise)
Low-speed shaft (LLS) bending moment	Magnitude of the combined low-speed shaft bending moment in the two transverse directions at the rotating hub
Tower base bending moment	Magnitude of the combined fore-aft and side-to-side bending moment at the tower base
Tower base torsional moment	Magnitude of the torsional moment at the tower base

is a constant-amplitude load range that would, over the same number of cycles, cause an equivalent amount of damage as the original load series of variable amplitude.

To compute DELs, we use rainflow counting to extract the ranges and frequencies of the different load cycles. To be able to use our signals to compute DEL, we also need to correct it for the mean loads, which is accomplished by applying the Goodman correction. In other words, Goodman's correction take into account the mean loads to provide a more accurate calculation of the DELs. While the results shown here do have the Goodman correction, we note that such correction has not changed the results in any meaningful way, as the loading cycles resulted in stresses that were significantly lower than the ultimate stresses of the material of each component. That is to be expected since the turbine is operating far from the edges of its operational envelope. The Goodman-corrected DEL are then used to directly compare the different simulation scenarios. No lifetime fatigue calculations are shown because it is not applicable to the single condition under investigation.

As noted in Table 1, the magnitude of two orthogonal signals are used for the tower-base, low-speed shaft, and blade-root bending moments. We compute load roses for each pair of these signals and come up with single signals for each sector around the load rose. We use sectors of 10 degrees each and obtain the time series. The entire workflow of obtaining both the standard deviation and DEL are then executed for each sector and the highest value is taken as the standard deviation or DEL of that signal. This approach is taken for three pairs of signals: tower-base fore-aft and side-to-side bending moment; blade-root in-plane and out-of-plane bending moment (flapwise and edgewise); and low-speed shaft bending moment across the two orthogonal directions.

The short-term DELs, referred to as simply DELs, are computed as

$$\mathrm{DEL} = \left(\frac{1}{T} \sum_k n_k L_k^m \right)^{1/m} \tag{1}$$

where n_k is the number of cycles of some load L_k related to load bin k (after applying the Goodman correction), m is the slope of the Whöler curve of the material, and T is the total length of a given simulation representing a 1 Hz-equivalent cycle (that is, T is the number of 1-Hz cycles over the simulation). The bins k are obtained using the load ranges obtained using rainflow counting of the Goodman-corrected time-series of stresses. We first convert loads to stresses using material properties and then apply Goodman's correction on the stresses. The resulting stresses are converted back to loads and used in the DEL calculations.

In our load analysis, we assume axial stresses only, with the bending moments being the contributing load towards this axial stress in each turbine component. We also assume the geometry of the blade root is of uniform circular cross section. We do consider material ultimate strength separately for each turbine component and pick the worse value (from tension and compression), yielding possibly conservative results. We do not perform further analysis to take the non-isotropic composite materials into account for our load analysis. The ultimate stresses used to correct for mean loads using Goodman were $1,047$ MPa for the composite blade root, 814 MPa for ASTM 4140 drivetrain steel used for the low-speed shaft, and 450 MPa for ASTM A572 steel used for the tower. We have used a Wöhler exponent of 4 for steel components and 10 for the composite blade.

3 Calibration of the curled wake model

190 To ensure that wake meandering characteristics, and thus loading of downstream turbines, are as accurate as they can be when running analysis using FAST.Farm, we first perform a calibration against the LES solutions. The calibration encompasses varying key parameters in the wake models and comparing the resulting quantities with LES. The LES runs included the turbines using the actuator line model, and 3 yaw conditions were executed: positive, negative, and no yaw. The positive yaw case had a reference yaw $\gamma = 20$ degrees, (meaning $\gamma_{T1} = \gamma_{T2} = \gamma_{T3} = 20$ degrees, $\gamma_{T4} = 10$ degrees and $\gamma_{T5} = 0$). The

195 negative yaw had the same magnitudes (with the sign flipped), and all turbines were aligned (zero yaw) for the no-yaw case.

We performed the workflow described in this section for both the polar wake and the curled wake models of FAST.Farm. The polar wake model is a simpler axisymmetric model and two constants were used for tuning. The constants are related to the wake propagation angle and initial offset that are proportional to yaw misalignment (respectively called `C_HWkDfl_xY` and `C_HWkDfl_OY` in FAST.Farm). The curled wake model (Martínez-Tossas et al., 2021) is a more realistic model that takes

200 into consideration the curled vorticity present in skewed flow and the rotor rotation, yielding a wake that is curled, resembling a "kidney shape". For the curled wake model, two additional constants are considered in the calibration: one related to the decay rate of the spanwise velocity components (`k_VortexDecay` in FAST.Farm), and another related to the scaling of the eddy viscosity, which effectively controls the amount of diffusion in the model (`k_vCurl` in FAST.Farm). For our cases of interest, we perform sweeps on all of these constants for the IEA Wind 15-MW reference wind turbine under neutrally stratified

205 inflow generated in LES (described above). Our approach consisted of setting a series of sweeps, analyzing the results, and setting up another series of sweeps around the best performing values, narrowing the range of values closer to the optimal ones observed in prior sweeps. In this way, we effectively increased the resolution of the final parameters without having to execute an unnecessarily large number of cases. A table showing all sweeps and ranges of each parameter for the curled wake calibration is shown in Table 2. A total of 4,500 FAST.Farm simulations were executed and analyzed to come up with the

210 optimal parameters for the curled wake model that are used in the rest of this work. A similar set of cases were used to calibrate the polar wake model.

Table 2. Range of the sweeps of curled wake modeling parameters within FAST.Farm for calibration procedure. Each case was executed under 3 different yaw conditions and compared with its respective LES solution.

	Sweep 1		Sweep 2		Sweep 3		Sweep 4	
	min	max	min	max	min	max	min	max
`C_HWkDfl_OY`	0.1	0.5	0.0	0.3	0	0.3	0	0
`C_HWkDfl_xY`	-0.008	-0.002	-0.006	0	-0.006	0	0	0
`k_VortexDecay`	0	1	0	0.4	0	0.4	0	0.04
`k_vCurl`	1	5	1	5	1	5	1	5
Number of cases	1260		1134		1944		162	

The quantities used for the comparison and to determine which combination of wake parameters performed best are generated power and the lateral wake center behind each turbine. Transverse, vertical planes of inflow are saved at 2, 3, 4, 5, and 6 diameters downstream of each turbine for each of the 3 LES cases and each FAST.Farm case shown in Table 2. From those planes, wake centers are identified using a 1-D Gaussian fit (Quon et al., 2020). For illustration purposes, an example of a time-series between LES and FAST.Farm for the no-yaw case is shown in Figure 5. Note how, as expected, the error due to the dynamic wake meandering model increases with increasing downstream distances.
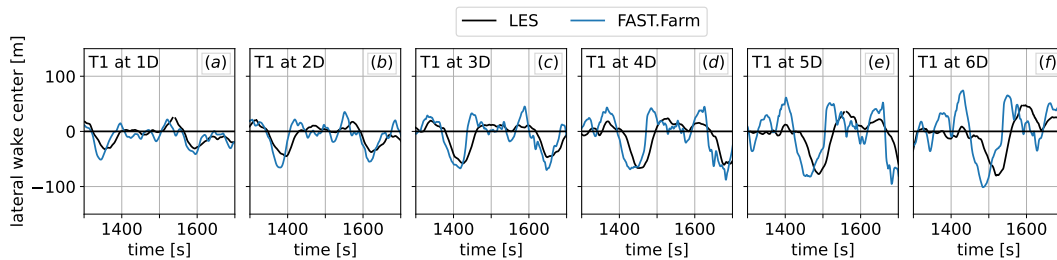
Figure 5. Illustration of the time-series for the lateral wake center for both FAST.Farm and LES. The FAST.Farm data shown is related to optimal values for the polar wake model.

Differently from prior studies (e.g. Shaler and Jonkman (2021)), we devised a simple wake center error metric that takes into account time-accuracy and not just mean wake center. We compare LES and FAST.Farm at every second and then get the mean error. The metric that was minimized is given by $\Delta \overline{y} = \overline{|y_{\mathrm{FF}} - y_{\mathrm{LES}}|}/D$ where y corresponds to the time series of the lateral location of the wake and D is the rotor diameter. A similar power metric is used, $\Delta \overline{P} = |\overline{P}_{\mathrm{FF}} - \overline{P}_{\mathrm{LES}}|/|\overline{P}_{\mathrm{LES}}|$.

Here we skip much of the details of earlier sweeps and provide two intermediate results to give the reader a sense of the quantities and cases compared. For the third sweep indicated in Table 2, we can plot the four-dimensional wake center difference $\Delta \overline{y}$ dataset as shown in Figure 6. Note how for every combination of the four parameters, a zero-valued C_HWkDfl_xY is consistently better (darker shades within each sub-plot). Also, for each subplot, minimal variation of C_HWkDfl_OY is observed. From that, we picked our two wake deflection parameters to be zero on the fourth sweep. Additionally, observing each individual row, results improved as we move towards the bottom rows (lower k_vortexDecay), suggesting we should focus on lower values for this variable.

There is a balance between choosing the case that yield best performance in terms of wake center and the case that is best for matching power. In Figure 6, little variation is observed across the different columns of sub-plots (varying k_vCurl). However, if we create the same plots for the power metric, it is clear an optimal k_vCurl exists—see Figure 7.

Figures 6 and 7, however, only show a single yaw case. Another balance has to be considered across all three yaw scenarios, since this is the goal of this study. On sweep four, we are able to reduce the number of variables we are varying and make ensemble averaged plots, considering 3 downstream planes of the first turbine (at 4, 5, and 6 D) and average them together. These average plots are shown in Figure 8, representing the fourth and final sweep considered in this work.
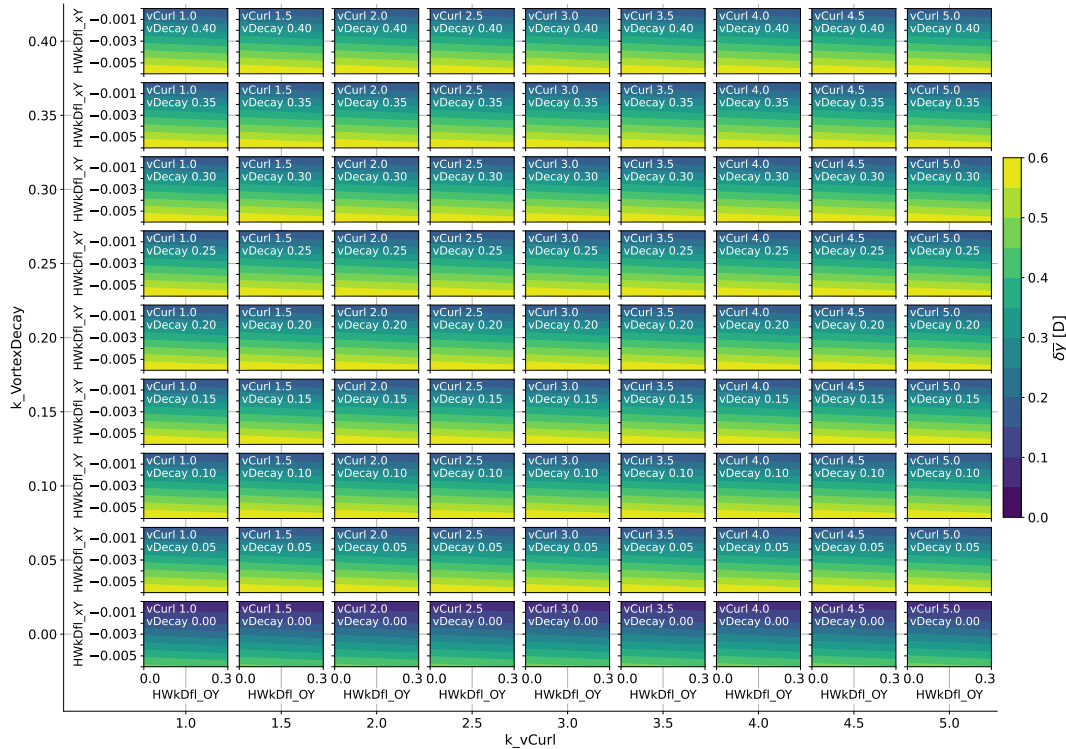
Figure 6. Differences between the wake center obtained through FAST.Farm and those obtained using LES for the zero yaw case. Shown are the values related to sweep 3 from Table 2. Each small subplot is a function of the two wake deflection parameters, while the outer-most axis vary in the other two curled wake parameters. Darker shades mean such constants performed best.

Different optimal values exist between the different yaw configurations, but with the goal of picking single values for all yaw scenarios (so as to not overfit the LES data), the final values chosen strike a balance between all three yaw cases (positive, negative, and zero yaw) and both quantities of interest (power and wake center). For instance, wake location is much less sensitive to the value of `k_vCurl` than power, so we prioritize values in which power matched better. The optimal of
240 `k_vCurl` for power vary depending on the yaw configuration. In this work we prioritize yawed turbines, so we focus on the results from Figure 8(e) and (g). We pick the final value as 5 as the negative yaw scenario is less sensitive to its value than the positive yaw case. Final values are given in Table 3. In the final table, for the purposes of generality, we also provide the optimal values for the polar wake model (steps not shown in this article).

We note that the calibration procedure outlined above applies to the fixed-bottom IEA Wind 15-MW reference wind turbine
245 for the conditions of interest in this work. The steps could be reconsidered for different conditions and turbines, although it is not clear if the values are sensitive to condition or turbine. For illustration purposes, we finish this section by showing a flowfield picture comparing the LES and the equivalent FAST.Farm case with the calibrated parameters for the curled wake model—Figure 9.
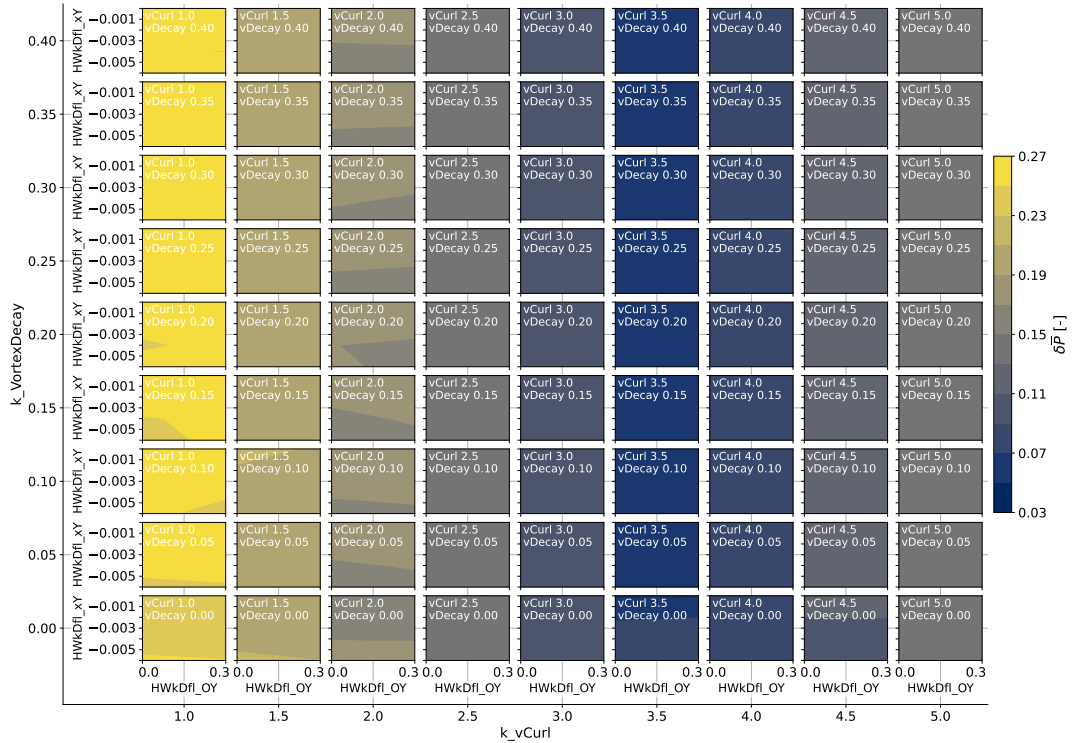
Figure 7. Differences between total power obtained through FAST.Farm and those obtained using LES for the zero yaw case. Note how for this sweep, a optimal `k_vCurl` of around 3.5 exists.
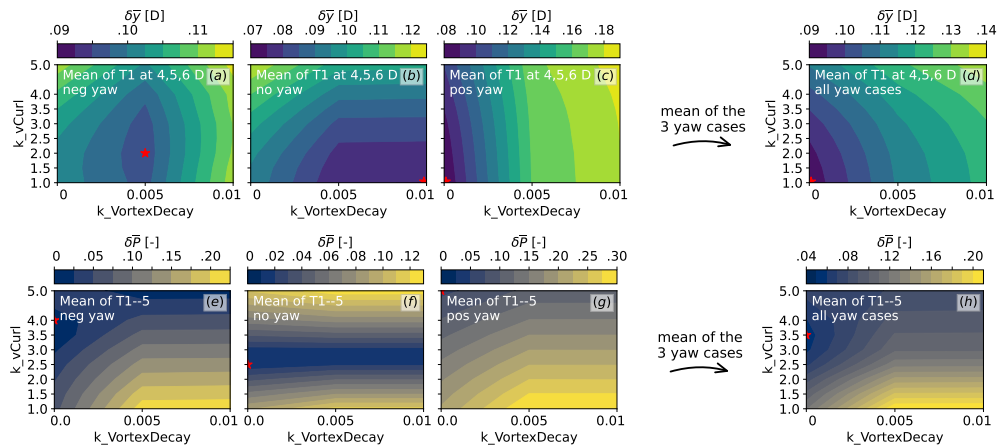
Figure 8. Differences in wake position (a–d) and power (e–g) between FAST.Farm and LES for each yaw condition, as indicated in each sub-plot. The red mark represents the optimal point of each scenario and each quantity of interest. Mean of each quantity shown in (d) and (h).

Table 3. Final calibrated FAST.Farm parameters for the IEA Wind 15-MW fixed-bottom reference wind turbine. Default values also shown for reference.

	Polar		Curled	
	Default	Calibrated	Default	Calibrated
C_HWkDfl_OY [m/deg]	0.3	0.3	0	0
C_HWkDfl_xY [deg^{-1}]	-0.004	-0.006	0	0
k_VortexDecay [$-$]	—	—	0	0
k_vCurl [$-$]	—	—	2	5
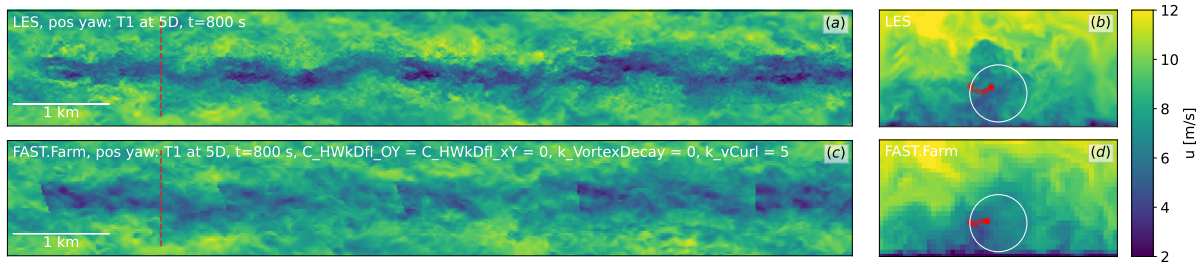
Figure 9. A snapshot of the positive-yaw case of LES and FAST.Farm for the calibrated curled wake solution. Note how the background flow is the same. The wake plane at 5D of the first turbine, indicated by the red dotted line, is shown on the right. The wake center at the time instant shown, as well as a 50-second history, is indicated by red dots on the wake plane panels.

4 Results

250 We present the results of all the cases in terms of contour plots, or, "heat maps", which includes sweeps in terms of both wind direction and yaw angle. In the figures that follow, the vertical axis varies with respect to the reference yaw γ, while the horizontal axis represents the wind direction. The baseline (reference) case is at the center of the plot, with the no-yaw, aligned-wind case ($\alpha = \gamma = 0$). We will refer to the four resulting quadrants, representing combinations of wind direction and reference yaw angle.

4.1 Effects on Wind Farm Power

The power gains and losses are shown for each turbine and each condition in Figure 10(a–e). For each turbine, we normalize the power by the power of the leading turbine at the baseline no-yaw, aligned-wind scenario. Such normalization means that non-leading, downstream turbines will generally have a normalize power value lower than unity due to the upstream wake effects. Figure 10(f) shows an average of the 5 turbines.

260 Figure 10 contain a lot of information, and it can be difficult to understand all of it at first. To provide the reader a more intuitive way of understanding this figure and subsequent ones, we show the same data for the 3 indicated points differently.
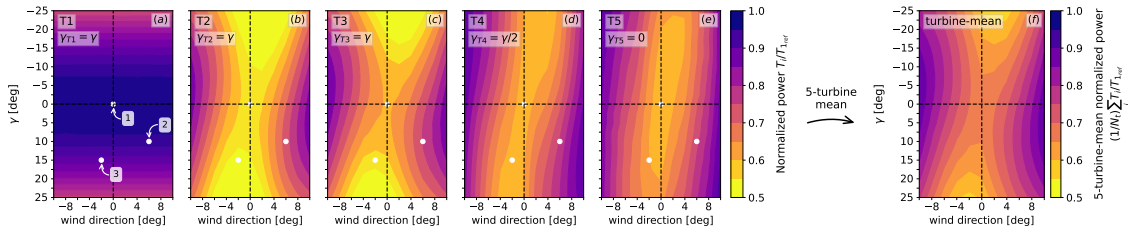
Figure 10. Normalized power for each turbine under each configuration investigated. For each individual turbine, (a–e), power of turbine i is normalized by the baseline power of the leading turbine, $P(T_i/T_{1_{\text{ref}}})$. Turbine-mean results are shown in (f). The same data at points indicated by 1, 2, and 3 are shown in Figure 11.

Taking the values of the contours from Figure 10 of the 3 points, we obtain Figure 11 showing the power down the row. The power normalization choice becomes more intuitive now. Point 2 is shown to generate more total farm-wide power than the baseline case (point 1) and point 3.
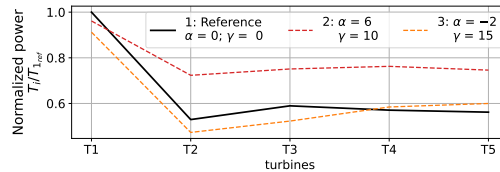
Figure 11. Normalized power down the row for selected cases, showing typical behavior of power loss on waked turbines. As indicated in the legend, each curve is related to each of the points 1, 2, and 3 from Figure 10.

265 The average power of each case is shown in Figure 10(f), but it is difficult to visualize the relative differences with respect to the baseline case. Let us now take the turbine-mean normalized power from Figure 10(f) and normalize by its baseline case, shown in Figure 12. Using such normalization allows us to see which farm configurations provide a power gain with respect to the baseline case, where no wake steering strategy is employed.

Figure 12 shows that power gains can exceed 35% in certain scenarios (shown by point 6), while power losses can also be
270 observed (e.g. point 4). To relate the power gains to the actual configuration, we visualize 3 arbitrary points of the domain. For point 4, Figure 12(b), the turbines are highly yawed in the negative direction, while the wind is at a slightly positive ($\alpha = 2$) inflow direction. In this case, as the turbines yaw to steer the wake away from downstream turbines, the wind direction brings the wake back directly into the rotor of downstream turbines, making wake steering highly ineffective. The loss in power is noted by the blue color. Such scenarios are not the goal and are a consequence of the full sweep of variables performed. On
275 the other hand, the condition noted by point 5, Figure 12(c), is a realistic combination of wind direction and yaw angle, and it yields a power gain of about 13% with respect to the baseline case. Finally, the regions of dark red color are the conditions of highest power gain, which are related to highly skewed flow, naturally diverting most of the wake by itself. This is clearly illustrated in Figure 12(d), on a condition of $\alpha = 10$ degrees with $\gamma = 7.5$ degrees. While the power gains obtained by dark red areas are operationally attractive, as will be shown in the next section, this comes with significantly increased fatigue loads,
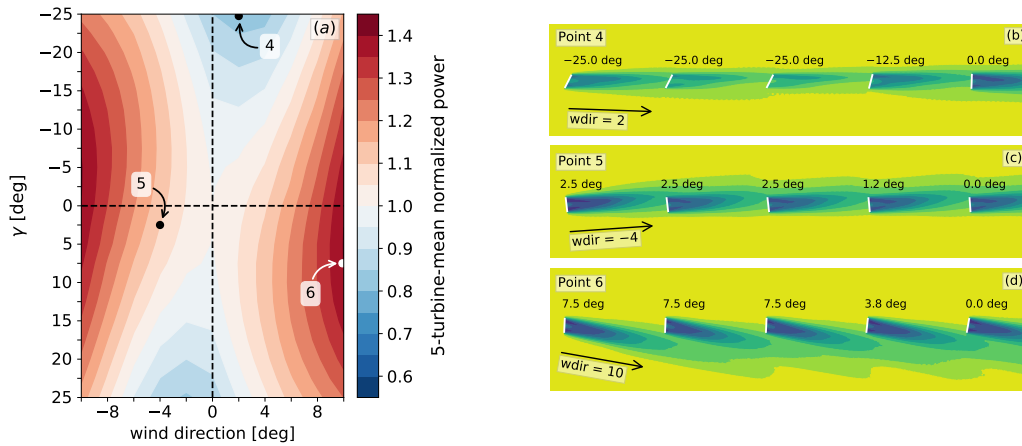
Figure 12. Farm-mean power (Figure 10(f)) normalized by the power of the baseline no-yaw aligned wind case (point 1 in Figure 10(a)). Power variation exceeds 35% of the baseline power. Time-averaged flowfield of points 4, 5, and 6 indicated are shown on right, (a,b,c).

280 rendering such condition unrealistic. This is an important observation as it showcases the need to perform performance studies with wake steering alongside structural fatigue load analysis.

We note that a wind farm operator that has control over the turbine configurations (but not the wind) can use charts like the ones presented in Figures 10 and 12 to estimate power changes given certain yaw angle configurations.

While Figure 12(a) appears symmetric at first, we can compute the differences between the positive and negative yaws in 285 terms of power. Here we introduce the idea of splitting the results in terms of the four quadrants, as separated by the dashed lines at $\alpha = 0$ and $\gamma = 0$. To establish a direct comparison, we split Figure 12(a) in half horizontally, at $\gamma = 0$. We obtain the differences between positive and negative yaw by taking the bottom two quadrants (positive yaw) and comparing against a mirrored version of the top two quadrants (negative yaw). Figure 13 shows the approach. Panel (a) shows the bottom two quadrants and panel (b) shows the top two quadrants, mirrored. Panel (c) shows the differences in terms of absolute percentage 290 when compared to the baseline case.
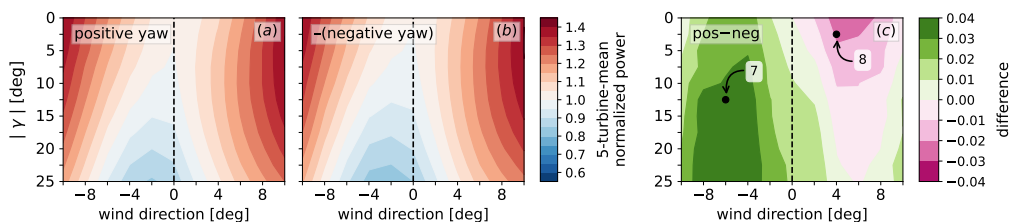
Figure 13. Asymmetry differences between positive and negative yaw cases. (a) Positive yaw contour map, the same as the bottom part of Figure 12; (b) negative yaw contour map, mirrored from the top part of Figure 12; (c) difference in terms of power between positive and negative yaw. In the (c) panel, for winds and yaw of opposite sign, positive yaw is up to $\sim 4\%$ better (green on the left side of (c)), while for winds and yaw of the same sign, negative winds and yaw yields up to $\sim 2\%$ more power (pink part on the right side of (c)). Points noted by 7 and 8 in (c) are shown in Figures 14 and 15, respectively.

Regarding Figure 13(c), the green left side means negative wind and positive yaw yields more power than its symmetric counter-part, positive wind and negative yaw, for all conditions. In other words, the bottom left quadrant overperforms top-right quadrant. The mostly-pink right side means the bottom-left underperforms the top left quadrant—that is, for wind and yaw of the same sign, positive values are up to 2.2% worse. For aligned wind ($\alpha = 0$ line), a positive yaw always results in more power than a negative yaw of the same magnitude. More intuitive visual schematics for points 7 and 8 of Figure 13(c) are presented in Figures 14–15, respectively.
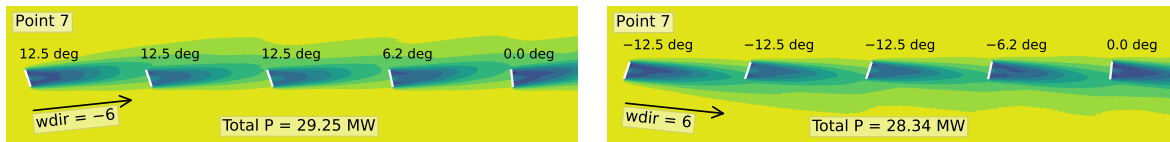
Figure 14. Visual schematic of the dark green point noted as 7 in Figure 13(c). Negative wind direction with positive yaw angles generates 3.2% more power than its symmetric scenario.
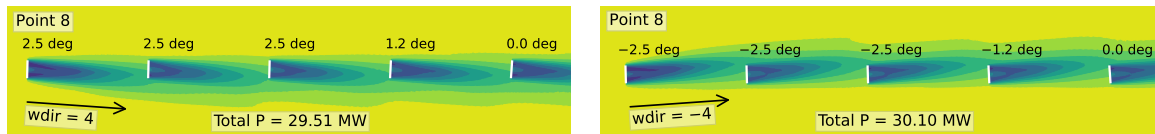
Figure 15. Visual schematic of the dark pink point noted as 8 in Figure 13(c). Positive wind direction with positive yaw angles generates 2.2% less power than its symmetric scenario.

4.2 Effects on Wind Farm Loads

Load characteristics for each individual turbine and farm-mean are presented in this section. We will focus on the load channels outlined in Table 1, processed as discussed in Section 2.4. In all of the plots shown in this section, the colorscale has two values. One of them is the absolute value of the quantity being shown, while the second is a percent change from the baseline (indicated by "BL"), which is the leading turbine, no-yaw, aligned-wind case. The percent scale allows us to identify relevant changes, while the absolute scale captures the severity of the change. We will focus on the areas of positive net gain in power, to assess their corresponding impact on loads, and relate our findings to the four quadrants of the contour plots.

The times-series mean loads are shown in Figure 16, where each row shows one channel for each individual turbine as well as a turbine-mean load map. First, and as expected, the leading turbine sees vastly different characteristics due to its unwaked condition, and for any given yaw misalignment γ, the loads remain constant across wind directions. The tower-base torsional moment exhibits asymmetries, and has the lowest mean at around $\gamma = 12$ degrees. The blade-root and tower-base mean bending moments are highest for the baseline case. The mean low-speed shaft bending moments in a rotating frame of reference are nearly zero for all cases (as expected). For the downstream, waked turbines, mean blade root and tower base loads for waked turbines follow more or less the trends of the power map. The magnitude of the mean for the tower torsional moment

shows signs of asymmetry for the waked turbines too, in which the conditions within the bottom right quadrant (positive wind direction and positive yaw) result in the lowest mean loads.
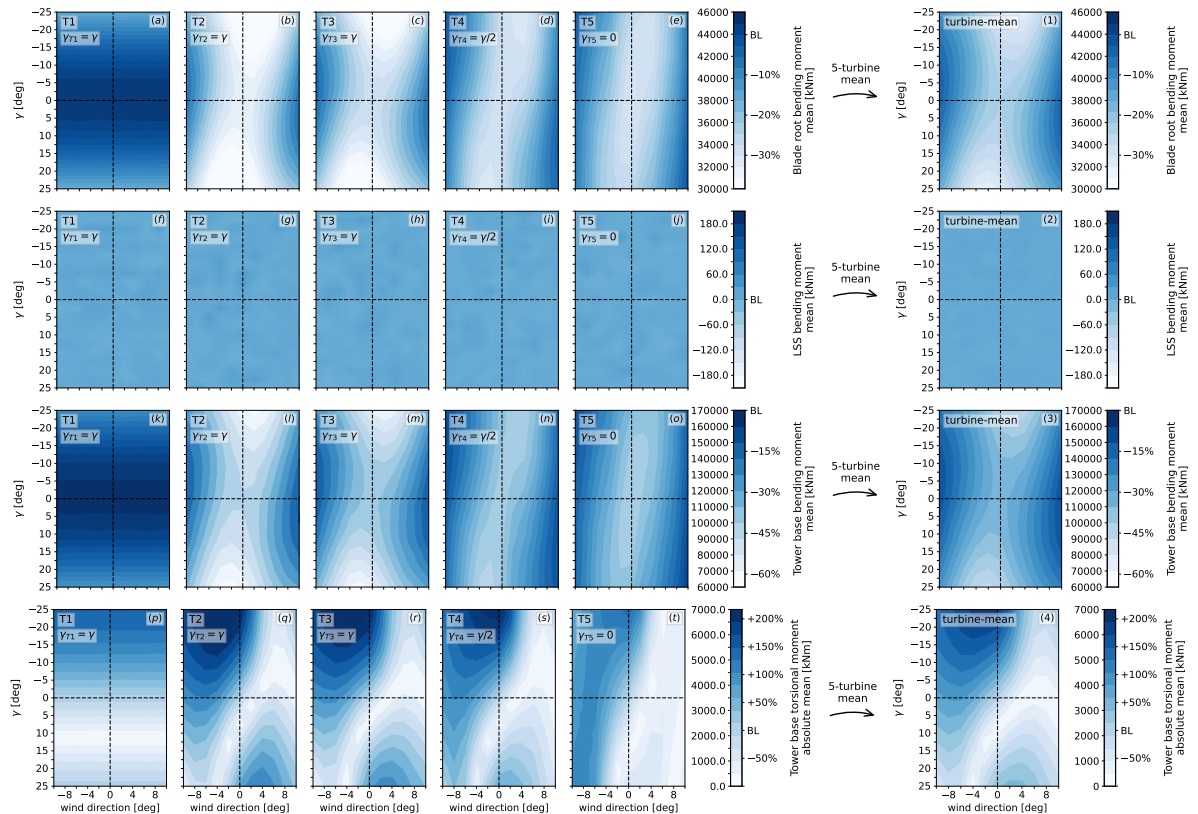
Figure 16. Mean of the load channels of interest for each turbine. One channel per row; note different scales for each channel. Note how some of channels monotonically increase. Low-speed shaft bending moment mean is nearly zero, as expected.

Next we show in Figure 17 the standard deviation of the load channels in the same fashion. Standard deviation is often more intuitive than DEL, can be considered as a proxy for fatigue loads, and offers more insight into the asymmetries than

315 the mean loads. For the blade-root and LSS bending moments, for any given wind direction and any turbine, the load standard deviations are monotonically increasing from positive to negative yaw angle. Such a monotonic behavior has been observed in both simulation and measured data (Damiani et al., 2018) and are attributed to gravity loading being relieved by aerodynamic loading as the yaw goes from negative to positive. For both channels, the bottom right quadrant (positive wind direction and positive yaw) incurs the lowest standard deviation. Reductions of 4 to 6% can be observed for the blade-root bending moment,

320 and up to 20% for the LSS. Analogously, $\sim 4\%$ higher load standard deviations for the blade-root bending moment and up to 30% for the LSS are seen in the worst performing quadrant (negative wind direction and negative yaw). For these two channels, for any given wind direction, the more positive the yaw, the better. For example, for aligned-wind situations, a certain positive yaw, γ, will generally reduce the standard deviations with respect to no-yaw, while a negative yaw, $-\gamma$, will increase it.
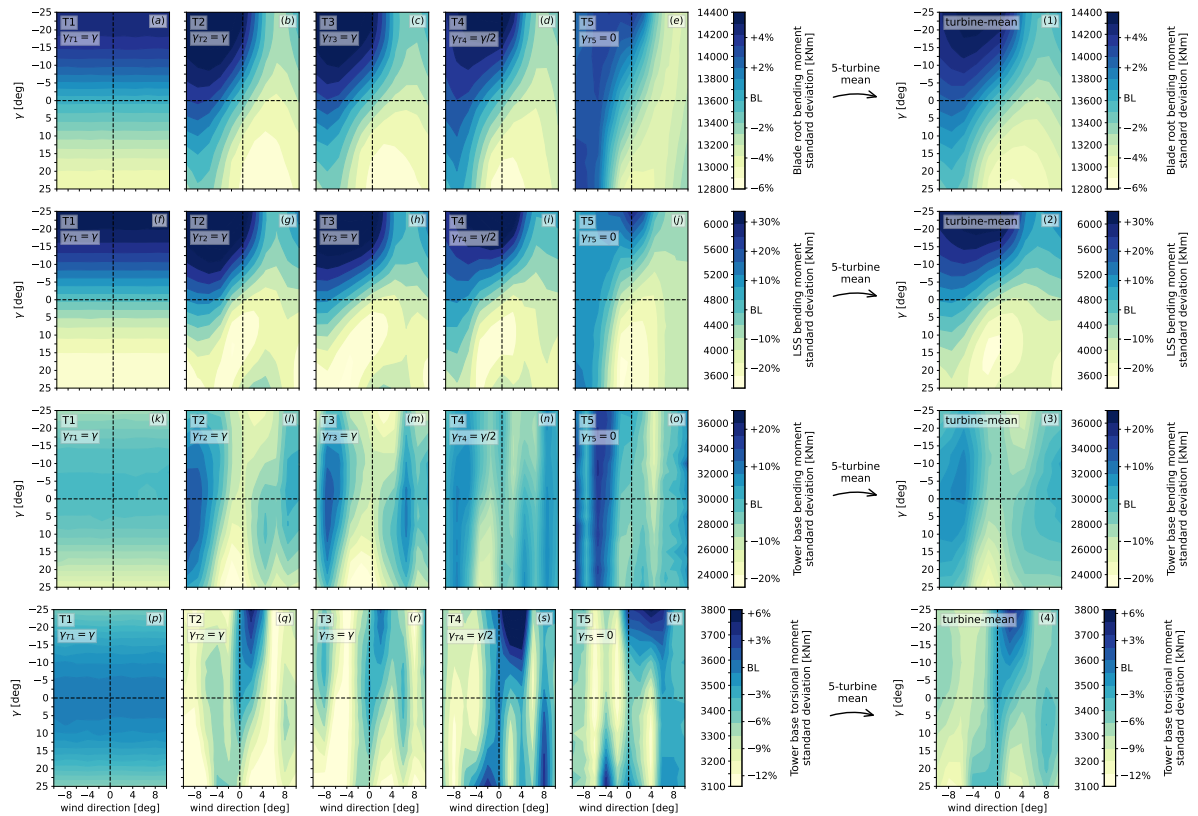
Figure 17. Standard deviation of the load channels of interest for each turbine. One channel per row; note different scales for each channel. The standard deviation of low-speed shaft (f–j) and tower base (k–o) bending moments are the most sensitive to the yaw and wind direction conditions investigated.

Non-monotonic, more complex trends in standard deviation are seen for the tower-base bending and torsional moments.
For the tower-base bending moment, the conditions of low standard deviation (yellow regions in turbine-mean map, panel (3) of Figure 17) are the same conditions of overall power losses and thus undesirable. Excluding those conditions from our analysis, the same bottom right quadrant (positive wind direction and positive yaw) is the best performing, the top left (negative wind direction and negative yaw) is the worst performing. Regarding the tower-base torsional moment, areas of low standard deviation are observed for negative wind directions, where positive yaw condition is better than negative. For all the channels shown, between the two symmetric top right and bottom left quadrants, the bottom left quadrant (negative wind direction and positive yaw) generally yields lower values of standard deviation, suggesting they incur lower fatigue damage. In general, the LSS bending moment and the tower-base bending moment are the two channels with the largest sensitivity, resulting in larger increases/decreases when compared to baseline cases.

The two channels noted above with significant standard deviation are the same channels with the highest relative variation in short-term DEL, as shown in Figure 18. In general, the trends observed in the standard deviations are very similar to ones seen

here for DELs, with a clear correlation between the two quantities. An exception is the tower-base torsional moment, where the downstream turbines see significantly lower values of DELs when compared to the leading turbine. The turbine-mean contours are similar to the standard deviations, and the cases with the lowest DELs are those from the bottom right quadrant for the blade-root, LSS, and tower-base bending moments, when excluding the areas of net loss in power (the blue shades of Figure 12(a)).
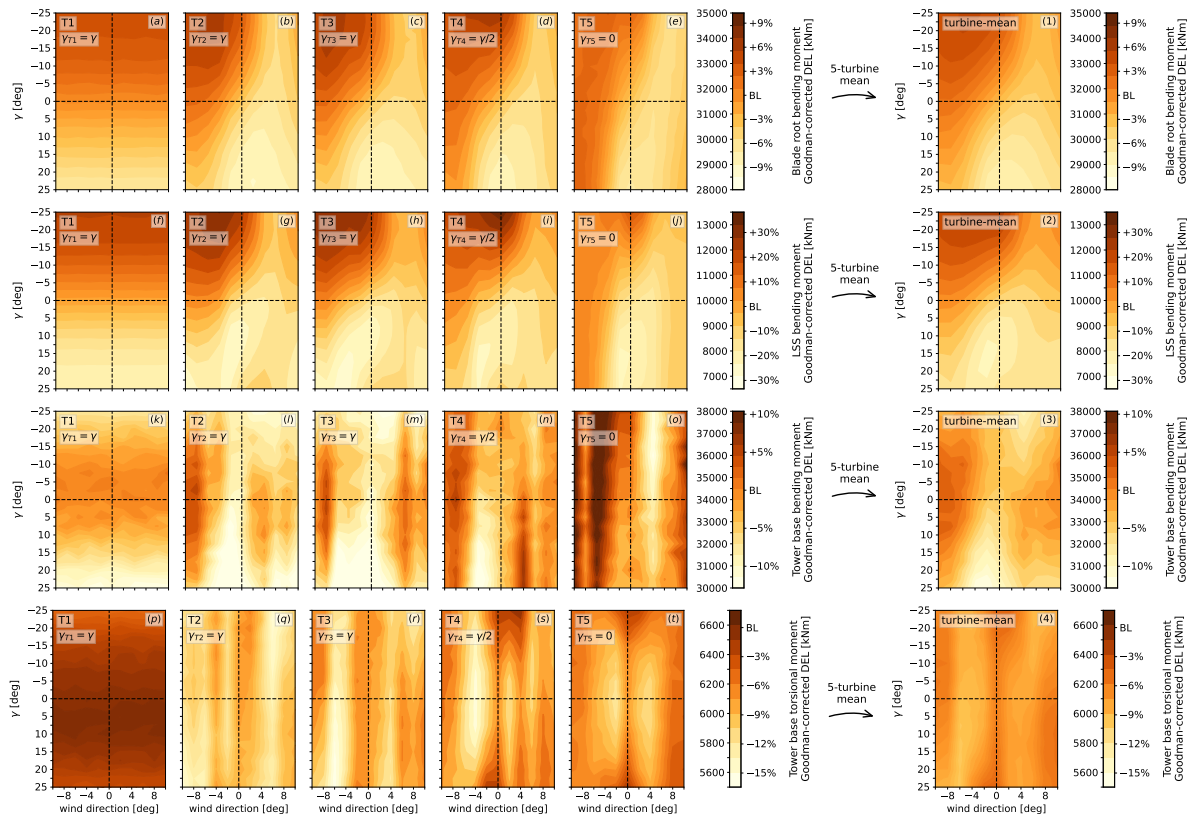
Figure 18. Short-term DELs including Goodman correction for the load channels of interest for each turbine. Note different scale for each channel.

4.3 Asymmetries and Partial Waking

Partially waked conditions are known to play a role in load fluctuations experienced by the blades. If the wake is prominently hitting the rising blade, then an increase in load fluctuations will be observed. Similarly, if the wake is prominently reaching the falling blade, lower fluctuations in loads can be seen. This was explained nicely by Stanley et al. (2020) and is confirmed here with the additional context of positive versus negative yaw angles.

To help explain the differences observed in terms of symmetry, let us pick two pairs of cases. The first is with wind direction ± 2 and $|\gamma| = 7.5$ degrees, in which a variation of plus or minus 2% in the standard deviation of the blade root bending moment

loads is observed (Figure 17(a–e)). A second case is more extreme, where differences will be more evident: wind direction ± 4 and $|\gamma| = 20$ degrees, which gives a load variation of more than 6% with respect to the baseline case. We will use these two pairs to highlight partial waking and asymmetry in loads. The two scenarios are illustrated in Figs. 19–20.
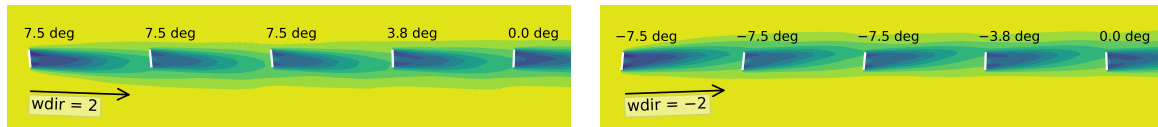
Figure 19. Flowfield of symmetric cases where partial waking plays a role.
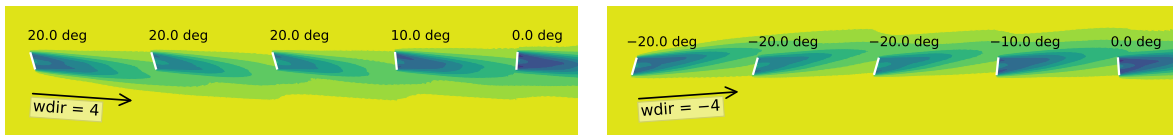
Figure 20. Flowfield of symmetric cases where partial waking plays a more significant role. The yaw angles and wind direction combinations might not be realistic.

During partial wake conditions, the blades passing through the waked part of the rotor are subject to smaller aerodynamic loading due to reduced freestream wind speed. In both Figs. 19–20, the positive yaw and positive wind direction cases have the wake reaching the downstream turbines more on the falling side. At the falling side of the blade, gravitational loads have the same sign as the aerodynamic loading. Because gravitational loads have constant amplitude, the smaller aerodynamic load on the falling side results in overall smaller loads, that is, cycles that have smaller peaks. In this situation of positive yaw, the rising blades see non-waked conditions, and thus higher loads, which are now opposite to the sign of the gravitational loads, resulting in smaller peaks of load magnitude for the rising blades. The opposite, analogous physics happen under negative yaw and negative wind direction conditions, resulting in overall larger peaks. For negative yaw cases, the wake is hitting the blades that are rising, reducing aerodynamic loads when aerodyanamics and gravity are opposite, resulting in larger magnitudes. Similarly, the non-waked, falling blades see higher-speed wind that produce aerodynamic loads with the same sign as gravitational loads, again resulting in cycles with larger peaks. This behavior is illustrated in Figure 21 for a small time-series shown in terms of revolutions of the rotor (a revolution starts with the blade pointing up) and an aggregate for the entire 20-min simulated in this work.

5 Discussion

We discuss the results in terms of the four quadrants of the contour plots shown. Figure 22 provides schematics of each of the four quadrants for reference.

Given the quadrants in Figure 22, a summary of the findings is given below for each quadrant:
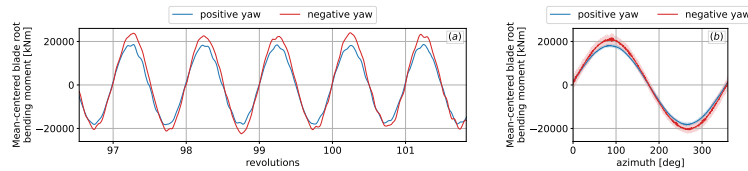
Figure 21. Mean-centered blade-root bending moments of the same symmetric case shown in Figs. 19–20. (a) Illustration of a short period of the time-series; (b) revolution-averaged quantities, with shaded region showing one standard devition from the mean.
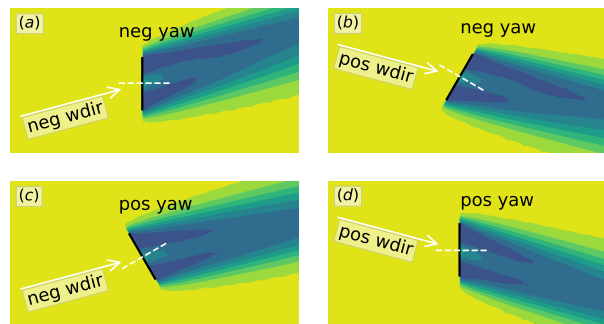
Figure 22. Schematic of the cases investigated. The figures are arranged in such a way that they correspond to the each of the four quadrants from prior images– (a) represents the top left quadrant; (b) the top right; (c) the bottom left; and (d) the bottom right

Figure 22(a):
- Represents the top left quadrant in the contour plots. Worst performing quadrant in terms of loads; worst performing quadrant overall.
- Consistent gain in power when compared to baseline case, up to 35%. Values are analogous to symmetric 22(d), as well we the exceptions described therein.
- Small gain in power (1–2%) compared to equivalent symmetric cases (bottom right quadrant).
- Significantly worse loads compared to its symmetric case. Blade loads standard deviation up to 9% higher and DEL up to 18% higher; LSS standard deviation up to 50% higher and DEL up to 50% higher; tower-base bending moment standard deviations up to 10% higher, while DEL up to 8% higher. Tower base torsional loads are about the same or sometimes slightly (less than 5%) better than its counterpart.

Figure 22(b):
- Represents the top right quadrant in the contour plots.
- Small values of wind direction ($\alpha \leq 4$ deg) and very negative values of yaw ($\gamma \leq -15$ deg) are undesirable, as the combination of wind and yaw result in the wake being steered directly into downstream turbines. These cases are the ones with loss in power with respect to the baseline case, thus loads and DEL information are not of interest in these cases.
- Power gains of up to 40% compared to the baseline case in the high wind direction $\alpha > 8$, small yaw angle $|\gamma| < 5$. Power losses are observed in undesirable configurations mentioned in the prior bullet point.

385

    – Power losses compared to its symmetric case can be observed for any given wind direction. The losses are the highest for wind $3 < \alpha < 9$ and $\gamma < -10$, up to 4%. They are the lowest for small wind directions $\alpha \leq 2$ and small yaw misalignment angles, up to $\gamma = -5$, where the losses are less than 1%.

    – For any given positive wind direction, blades and low-speed shaft loads (in terms of both standard deviation and DEL) increase monotonically from a lowest at no-yaw conditions. Tower-base bending and torsional moment standard deviation and DEL increase slightly depending on the magnitude of the yaw angle and wind direction.

390

    – Regarding its symmetric case, blade and tower bending moment are about 3% lower, LSS loads are 5–10% higher, depending on the combination of yaw angle and wind direction. Tower torsional moment are slightly lower (less than 3%) than its symmetric cases.

Figure 22(c):   – Represents bottom left quadrant in the contour plots.

395

    – Power gains of up to 38% compared to baseline case. Power losses can be observed under undesirable scenarios as noted in (a).

    – Power gains with respect to symmetric scenarios are between 1 and to 4%. Findings are analogous to findings from Figure 22(b) listed above.

Figure 22(d):   – Represents the bottom right quadrant in the contour plots. Best performing quadrant in terms of loads; best performing quadrant overall.

400

    – When compared to the baseline case, for yaw angles $\gamma < 15$ degrees, a power gain of up to 35% is observed for wind direction $\alpha = 10$ degrees, and up to 20% gain for wind direction $\alpha = 4$ degrees. For very large yaw angles $\gamma > 18$ degrees and small wind directions $\alpha < 2$ degrees, the undesirable situation of power loss is observed.

405

    – Compared to equivalent symmetric scenario: 1–2% loss in power.

    – For positive yaw angles, up to 5% lower standard deviation and 9% lower DEL is seen for the blade-root bending moment and up to 20% lower standard deviation and 25% lower DEL for the LSS (both with respect to their baseline case). Standard deviation for the tower-base bending moment are within 5% of its baseline, and DELs 2%, depending on the wind direction. The tower-base torsional moment standard deviation is up to 9% lower and DEL is at least 5% lower with respect to the baseline.

410

    – Compared to its symmetric counterpart, large benefits in terms of standard deviation and DELs for the blade-root bending moment and the LSS bending moment is present. Smaller differences are observed for the tower loads.

        The discussions above are given in terms of yaw angles and wind direction. We can interpret the results from a different point

415 of view. Operators can only control the yaw, so it is useful to summarize the findings in terms of wind directions. Considering only the regions of net positive power gain (red areas in Figure 12(a)):

- For any given positive wind direction: yaw $-2.5 < \gamma < 15$ degrees yields power gains of 10—20% over baseline. Positive yaw will incur lower blade root, LSS, and tower-base torsional standard deviation and DEL. Tower-base bending moment means and standard deviation follow the power map (higher power leads to higher loads). It is overall better to keep the turbine positively yawed.

- For any given negative wind direction: Positive yaw results in lower magnitudes for blade-root, LSS, tower-base bending, and tower torsional standard deviation and DEL values. With regards to tower-base torsion, negative yaw angles are preferred for inflow angles between 0 and -4 degrees, due to the loss in power if positive yaw in enforced. A loss in power of up to 2% is observed for positive yaws, but the gains in terms of loads may be significant enough to justify a positive yaw configuration for negative winds too.

6 Conclusions

In this work we have investigated yaw misalignment in a systematic way regarding positive and negative yaws with respect to wind directions varying from -10 to 10 degrees. We sought out to analyze data trends and physical driving mechanisms for power and loads asymmetries that have been previously reported.

In general, we have found that for positive wind directions, a positive yaw yields more power. For these conditions, lower positive yaw angles result in larger power gains. For the blade-root bending moment and LSS bending moment, the standard deviation and DELs are consistently lower for positive yaw angles when compared to its negative counterpart of same magnitude. For the tower-base loads, the trends are more complex but in general positive yaw still results in lower overall loads. For negative wind directions, positive yaw results in slightly less power than negative yaw, but the gains in terms of loads are significant. Blade-root and LSS bending moments have significantly lower loads in terms of standard deviation and DELs. Tower-base loads are comparable between positive and negative yaws.

The interplay of gravity and aerodynamic loading is the physical mechanisms driving some of the asymmetries observed. This interplay can be triggered in at least two ways observed in our simulations. First, by yaw angles that present either the rising or falling blade to the incoming wind. Second, by partial waking that reduces the inflow wind velocity on either the rising or falling half of the rotor plane. The latter mechanism was evidenced by flowfield visualization and time-series analysis of blade-root bending moment channels.

For the wind condition and the farm layout investigated in this work, and any wind direction, yawing the turbine in the positive direction is better than negative. While small power losses may incur ($\sim 2\%$), gains in terms of loads may be significant for farm operators. Finally, we note that the workflow used in this work could be easily adapted to investigate other conditions and farms of interest.

Code and data availability. Simulations were performed using AMR-Wind (available at github.com/exawind/amr-wind) and FAST.Farm (available at github.com/OpenFAST/openfast). Data shown in this work are available from the authors upon request.

Author contributions. RT: Conceptualization, methodology, investigation, formal analysis, software, validation, writing (original draft). GB: Conceptualization, supervision, writing (original draft, review and editing). JJ: Conceptualization, supervision, writing (review and editing)

450   RM: Validation, writing (review and editing) CB: Validation, writing (review and editing) KS: Conceptualization, writing (review and editing) JK: Conceptualization, supervision, writing (review and editing)

Competing interests. The authors declare no competing interests.

Acknowledgements. This work was authored in part by the National Renewable Energy Laboratory, operated by Alliance for Sustainable Energy, LLC, for the U.S. Department of Energy (DOE) under Contract No. DE-AC36-08GO28308. The views expressed in the article do

455   not necessarily represent the views of the DOE or the U.S. Government. The U.S. Government retains and the publisher, by accepting the article for publication, acknowledges that the U.S. Government retains a nonexclusive, paid-up, irrevocable, worldwide license to publish or reproduce the published form of this work, or allow others to do so, for U.S. Government purposes. This work was funded by Shell Global Solutions International B.V. under agreement ACT-1800038-5. The research was performed using computational resources sponsored by the Department of Energy's Office of Energy Efficiency and Renewable Energy and located at the National Renewable Energy Laboratory.

References

N. J. Abbas, D. S. Zalkind, L. Pao, and A. Wright. A reference open-source controller for fixed and floating offshore wind turbines. *Wind Energy Science*, 7(1):53–73, 2022.

M. Adaramola and P.-Å. Krogstad. Experimental investigation of wake effects on wind turbine performance. *Renewable Energy*, 36(8): 2078–2086, 2011. ISSN 0960-1481. https://doi.org/10.1016/j.renene.2011.01.024.

M. Bastankhah and F. Porté-Agel. Wind farm power optimization via yaw angle control: A wind tunnel study. *Journal of Renewable and Sustainable Energy*, 11(2), 2019.

M. Bastankhah and F. Porté-Agel. Experimental and theoretical study of wind turbine wakes in yawed conditions. *Journal of Fluid Mechanics*, 806:506—-541, 2016. https://doi.org/10.1017/jfm.2016.595.

U. Ciri, M. A. Rotea, and S. Leonardi. Effect of the turbine scale on yaw control. *Wind Energy*, 21(12):1395–1405, 2018. https://doi.org/10.1002/we.2262.

R. Damiani, S. Dana, J. Annoni, P. Fleming, J. Roadman, J. van Dam, and K. Dykes. Assessment of wind turbine component loads under yaw-offset conditions. *Wind Energy Science*, 3(1):173–189, 2018.

B. M. Doekemeijer, S. Kern, S. Maturu, S. Kanev, B. Salbert, J. Schreiber, F. Campagnolo, C. L. Bottasso, S. Schuler, F. Wilts, T. Neumann, G. Potenza, F. Calabretta, F. Fioretti, and J.-W. van Wingerden. Field experiment for open-loop yaw-based wake steering at a commercial onshore wind farm in italy. *Wind Energy Science Discussions*, 2020:1–22, 2020. https://doi.org/10.5194/wes-2020-80.

B. L. Ennis, J. R. White, and J. A. Paquette. Wind turbine blade load characterization under yaw offset at the swift facility. In *Journal of Physics: Conference Series*, volume 1037, page 052001. IOP Publishing, 2018.

P. Fleming, J. Annoni, J. J. Shah, L. Wang, S. Ananthan, Z. Zhang, K. Hutchings, P. Wang, W. Chen, and L. Chen. Field test of wake steering at an offshore wind farm. *Wind Energy Science*, 2(1):229–239, 2017. https://doi.org/10.5194/wes-2-229-2017.

P. Fleming, J. King, K. Dykes, E. Simley, J. Roadman, A. Scholbrock, P. Murphy, J. K. Lundquist, P. Moriarty, K. Fleming, et al. Initial results from a field campaign of wake steering applied at a commercial wind farm–part 1. *Wind Energy Science*, 4(2):273–285, 2019.

P. Fleming, J. King, E. Simley, J. Roadman, A. Scholbrock, P. Murphy, J. K. Lundquist, P. Moriarty, K. Fleming, J. van Dam, C. Bay, R. Mudafort, D. Jager, J. Skopek, M. Scott, B. Ryan, C. Guernsey, and D. Brake. Continued results from a field campaign of wake steering applied at a commercial wind farm – part 2. *Wind Energy Science*, 5(3):945–958, 2020. https://doi.org/10.5194/wes-5-945-2020.

P. A. Fleming, P. M. Gebraad, S. Lee, J.-W. van Wingerden, K. Johnson, M. Churchfield, J. Michalakes, P. Spalart, and P. Moriarty. Evaluating techniques for redirecting turbine wakes using SOWFA. *Renewable Energy*, 70:211–218, 2014.

E. Gaertner, J. Rinker, L. Sethuraman, F. Zahle, B. Anderson, G. E. Barter, N. J. Abbas, F. Meng, P. Bortolotti, W. Skrzypinski, et al. IEA wind TCP task 37: definition of the IEA 15-megawatt offshore reference wind turbine. Technical report, National Renewable Energy Lab.(NREL), Golden, CO (United States), 2020.

P. M. O. Gebraad, F. W. Teeuwisse, J. W. van Wingerden, P. A. Fleming, S. D. Ruben, J. R. Marden, and L. Y. Pao. Wind plant power optimization through yaw control using a parametric model for wake effects—a CFD simulation study. *Wind Energy*, 19(1):95–114, 2016. https://doi.org/10.1002/we.1822.

D. R. Houck. Review of wake management techniques for wind turbines. *Wind Energy*, n/a(n/a), 2021. https://doi.org/10.1002/we.2668.

P. Hulsman, M. Wosnik, V. Petrović, M. Hölling, and M. Kühn. Development of a curled wake of a yawed wind turbine under turbulent and sheared inflow. *Wind Energy Science*, 7(1):237–257, 2022. https://doi.org/10.5194/wes-7-237-2022.

Á. Jiménez, A. Crespo, and E. Migoya. Application of a les technique to characterize the wake deflection of a wind turbine in yaw. *Wind Energy*, 13(6):559–572, 2010. https://doi.org/10.1002/we.380.

J. M. Jonkman, J. Annoni, G. Hayman, B. Jonkman, and A. Purkayastha. Development of FAST.Farm: A new multi-physics engineering tool for wind-farm design and analysis. In *35th Wind Energy Symposium*, page 0454, 2017.

500 S. Kanev, E. Bot, and J. Giles. Wind farm loads under wake redirection control. *Energies*, 13(16), 2020. https://doi.org/10.3390/en13164088.

N. D. Kelley and B. J. Jonkman. Overview of the turbsim stochastic inflow turbulence simulator. Technical report, National Renewable Energy Lab.(NREL), Golden, CO (United States), 2005.

L. A. Martínez-Tossas, J. King, E. Quon, C. J. Bay, R. Mudafort, N. Hamilton, M. F. Howland, and P. A. Fleming. The curled wake model: a three-dimensional and extremely fast steady-state wake solver for wind plant flows. *Wind Energy Science*, 6(2):555–570, 2021.

505 D. Medici and P. H. Alfredsson. Measurements on a wind turbine wake: 3d effects and bluff body vortex shedding. *Wind Energy*, 9(3): 219–236, 2006. https://doi.org/10.1002/we.156.

D. Medici and J. Dahlberg. Potential improvement of wind turbine array efficiency by active wake control (awc). In *Proc. European Wind Energy Conference*, Madrid, Spain, 2003a.

D. Medici and J. Å. Dahlberg. Potential improvement of wind turbine array efficiency by active wake control (awc). In *Proceedings of European Wind Energy Conference*, pages 65—84, Madrid, Spain, 2003b.

510 E. Quon, P. Doubrawa, and M. Debnath. Comparison of rotor wake identification and characterization methods for the analysis of wake dynamics and evolution. In *Journal of Physics: Conference Series*, volume 1452, page 012070. IOP Publishing, 2020.

K. Shaler and J. Jonkman. Fast. farm development and validation of structural load prediction against large eddy simulations. *Wind Energy*, 24(5):428–449, 2021.

515 K. Shaler, J. Jonkman, G. E. Barter, J. J. Kreeft, and J. P. Muller. Loads assessment of a fixed-bottom offshore wind farm with wake steering. *Wind Energy*, 25(9):1530–1554, 2022.

E. Simley, P. Fleming, N. Girard, L. Alloin, E. Godefroy, and T. Duc. Results from a wake-steering experiment at a commercial wind plant: investigating the wind speed dependence of wake-steering performance. *Wind Energy Science*, 6(6):1427–1453, 2021.

M. A. Sprague, S. Ananthan, G. Vijayakumar, and M. Robinson. Exawind: A multifidelity modeling and simulation environment for wind energy. In *Journal of Physics: Conference Series*, volume 1452, page 012071. IOP Publishing, 2020.

520

A. P. J. Stanley, J. King, C. Bay, and A. Ning. A model to calculate fatigue damage caused by partial waking during wind farm optimization. *Wind Energy Science Discussions*, 2020:1–34, 2020. https://doi.org/10.5194/wes-2020-117.

J. Wagenaar, L. Machielse, and J. Schepers. Controlling wind in ecn's scaled wind farm. *Proc. Europe Premier Wind Energy Event*, pages 685–694, 2012.

525 D. S. Zalkind and L. Y. Pao. The fatigue loading effects of yaw control for wind plants. In *2016 American Control Conference (ACC)*, pages 537–542. IEEE, 2016.